

1 **UAS spherical photography for the vertical characterisation of canopy structural**
2 **traits**

3 Vicent Agustí Ribas Costa¹, Maxime Durand², T Matthew Robson² Albert Porcar-
4 Castell¹, Ilkka Korpela³, Jon Atherton¹

5 ¹Optics of Photosynthesis Laboratory, Institute for Atmospheric and Earth System
6 Research (INAR)/ Forest Sciences, Viikki Plant Science Centre (ViPS), Faculty of
7 Agriculture and Forestry, University of Helsinki, 00014, Finland; ² Organismal and
8 Evolutionary Biology (OEB), Viikki Plant Science Centre (ViPS), Faculty of Biological
9 and Environmental Sciences, University of Helsinki, 00014, Finland; ³ Institute for
10 Atmospheric and Earth System Research (INAR)/Forest Sciences, Faculty of Agriculture
11 and Forestry, University of Helsinki, 00014, Finland

12

13 **Author's Accepted Manuscript,**

14 New Phytologist, Methods paper, 26th January 2022

15

16

17

18 Author for correspondence:

19 *Jon Atherton*

20 Email: jon.atherton@helsinki.fi

21

22

23 Summary

24

- 25 • The plant area index (PAI) is a structural trait that succinctly parametrizes the
26 foliage distribution of a canopy and is usually estimated using indirect optical
27 techniques such as digital hemispherical photography. Critically, on-the-ground
28 photographic measurements forgo the vertical variation of canopy structure which
29 regulates the local light environment. Hence new approaches are sought for
30 vertical sampling of traits.
- 31 • We present an uncrewed aircraft system (UAS) spherical photographic method to
32 obtain structural traits throughout the depth of tree canopies. Our method
33 explained 89% of variation in PAI when compared with ground-based
34 hemispherical photography.
- 35 • When comparing UAS vertical trait profiles with airborne laser scanning data, we
36 found highest agreement in an open birch (*Betula pendula/pubescens*) canopy.
37 Minor disagreement was found in dense spruce (*Picea abies*) stands, especially in
38 the lower canopy.
- 39 • Our new method enables easy estimation of the vertical dimension of canopy
40 structural traits in previously inaccessible spaces. The method is affordable and
41 safe and therefore readily usable by plant scientists.

42

43 **Key words:** Spherical photography, uncrewed aircraft system (UAS), structural traits,
44 plant area index (PAI), plant area density (PAD).

45

46

47 Introduction

48 The vertical density of foliage relates to photosynthetic productivity by determining the
49 distribution and interception of sunlight through a plant canopy. As a measure of
50 vertically integrated foliage density, the leaf area index (LAI) is therefore an important
51 canopy structural trait and has been used to model a diverse range of processes including
52 photosynthesis (Duchemin *et al.*, 2006) evaporation and transpiration (Jongschaap, 2006;
53 Cleugh *et al.*, 2007) and rainfall interception (Dietz *et al.*, 2006).

54 Destructive measurement of LAI, generally defined as the one-sided leaf area per unit
55 area of ground (Zheng & Moskal, 2009), is laborious and impractical. Indirect optical
56 techniques including hemispherical photography are usually used instead (Jonckheere *et*
57 *al.*, 2004; Majasalmi, 2015). Indirect approaches typically invert the following model to
58 arrive at the LAI:

$$59 \quad P(\theta) = \exp\left(\frac{-G(\theta) \cdot \Omega(\theta) \cdot LAI}{\cos \theta}\right) \quad \text{Eqn. 1}$$

60 where $P(\theta)$ is the probability of a ray of light passing through the canopy without
61 encountering foliage or other plant elements at zenith angle θ , and G parameterises the
62 projection of leaf area relative to the zenith direction. It is the gap fraction $P(\theta)$ that is
63 measured by the optical instrument (Danson *et al.*, 2007). Clumping is accounted for with
64 the clumping parameter Ω (Nilson, 1971), however Eqn. 1 does not correct for woody
65 elements. In uncorrected form, the LAI is referred to as the plant area index (PAI) which
66 we use here (Chen *et al.*, 1991).

67 In digital hemispherical photography (DHP), a single lens reflex camera is combined with
68 a wide-angle lens, and possibly levelling equipment to ensure that the camera points
69 directly upwards or downwards (Guangjian *et al.*, 2019). Specialist software is used to
70 segment captured imagery into gap fraction or vegetation, and to derive structural traits
71 via Eqn. 1. Importantly, DHP has several limitations that if unaccounted for can produce
72 significant errors. Issues include the requirement for uniform, and usually overcast sky
73 conditions (Leblanc & Chen, 2001); sensitivity to camera settings and hardware,
74 including exposure (Macfarlane *et al.*, 2000), camera and lens types (Wagner, 1998),
75 image format and size (Frazer *et al.*, 2001); and choice of postprocessing steps, including
76 gamma correction (Macfarlane *et al.*, 2007) and segmentation algorithm (Nobis &
77 Hunziker, 2005). Recent work has shown how the use of raw format image files could
78 overcome some of these issues (Macfarlane *et al.*, 2014).

79 Despite the above limitations, DHP remains a popular option when field estimates of LAI
80 are required (Chianucci, 2020). However, it is an additional limitation that motivated the
81 development of the method described here; the restriction of sampling to on-the-ground
82 photography. This limits DHP to places accessible on foot, and more importantly
83 precludes measurement of vertical heterogeneity in canopy structure, a topic of much
84 interest to plant scientists (Disney, 2019). Note that it is the vertical plant area density
85 (PAD), or one-sided leaf area per unit volume (Hosoi & Omasa, 2006), that dictates the
86 local light environment (Smith *et al.*, 2019) and transfer of energy within a canopy (Lalic
87 & Mihalovic, 2004), and this is a trait that is unmeasurable from ground-based DHP.

88 For DHP to circumvent the on-the-ground restriction requires impractical structures such
89 as ropes (Fauset *et al.*, 2017), towers (Leuchner *et al.*, 2011; Dengel *et al.*, 2015), cranes

90 (Parker *et al.*, 2001), portable hydraulic hoists (Canham *et al.*, 1994) or balloons (Meir *et al.*,
91 *et al.*, 2000; Parker *et al.*, 2001), all of which can interfere with measurements. An
92 alternative approach is laser scanning technology, conducted using either airborne (ALS;
93 Korhonen *et al.*, 2011; Korpela *et al.*, 2014) or from terrestrial platforms (TLS; Calders
94 *et al.*, 2020). TLS (Hosoi & Omasa, 2006) or ALS (Lim *et al.*, 2003; Lovell *et al.*, 2003)
95 can be used to retrieve LAI and to model canopy light interception (Tian *et al.*, 2021a) in
96 three dimensions. However, the cost and complexity of laser scanning represent two
97 major drawbacks that prevent its widespread adoption. For plant scientists, laser scanning
98 systems have a high “barrier to entry” (Calders *et al.*, 2020).

99 Recently, uncrewed aircraft systems (UASs) have gained traction as platforms capable of
100 measuring spatial variation in canopy structure (McNeil *et al.*, 2016; Brüllhardt *et al.*,
101 2020; Krisanski *et al.*, 2020; Umarhadi & Danoedoro, 2021). Laser scanning
102 instrumentation can be mounted on UAS platforms to expand the horizons of ALS from
103 piloted aircraft to smaller, more manoeuvrable systems (Wallace *et al.*, 2012; Yin &
104 Wang, 2019; Brede *et al.*, 2019). A recent study demonstrated that within-canopy flight
105 is possible with a laser scanning UAS, although the UAS was relatively large and
106 therefore challenging and risky to fly in dense forest canopies (Hyypä *et al.*, 2021).
107 Additionally, recent studies have shown that above canopy ALS-like canopy trait
108 estimation algorithms can be applied to structure from motion photogrammetry data
109 collected from UAS platforms (Brüllhardt *et al.*, 2020; Lin *et al.*, 2021).

110 UAS-based DHP is also in active development, downwards looking in agricultural crop
111 fields (Brown *et al.*, 2020) and upwards looking in forest canopies (Brüllhardt *et al.*,
112 2020). The motivation for such systems is the low cost and complexity relative to laser
113 scanning systems, coupled with the access that an airborne system can provide. However,
114 and as with laser scanning, current UAS-DHP approaches require non-integrated imaging
115 systems and/or relatively large and heavy platforms. We developed the UAS-based
116 spherical photography method presented here to address these limitations. The new
117 method uses computational spherical photography and relies on standard cameras which
118 are integrated into mass-produced UAS airframes.

119 A panoramic spherical image is produced by combining multiple individual images to
120 cover an extremely large angle of view, up to and including the full viewing sphere. To
121 produce a panorama, individual images are algorithmically stitched together and mapped
122 onto a virtual spherical surface, that is subsequently reprojected onto the 2D plane
123 typically using the equirectangular projection (Zhang & Huang, 2021). Spherical
124 panoramas are acquired either with a combination of two wide-angle lenses via specially
125 designed cameras systems, or by rotating a conventional camera about its horizontal and
126 vertical axes whilst acquiring imagery (Fangi & Nardinocchi, 2013; Barbero-García *et al.*,
127 2018). In terms of plant science applications, spherical imagery has been used to
128 estimate individual tree heights, diameters at breast height, basal area and canopy
129 openness (Wang *et al.*, 2021). Spherical panoramas captured by a mobile phone have also
130 been used to reproduce gap fraction and LAI estimates from a traditional DHP system
131 (Andis-Arietta, 2021). In these studies, the spherical panoramas were reprojected to
132 hemispherical fish-eye projections, which are equivalent to imagery collected by DHP
133 systems.

134 In addition to mobile phones, panoramic photography is also possible using mass-
135 produced UASs. However most off-the-shelf systems cannot be readily used as a full 180°
136 vertical field of view is required, a feature that is relatively rare as it requires a specialized
137 gimbal capable of rotating the camera viewing direction upwards (see Fig. 1a. inset
138 drawing of UAS sensor). Our main goal was to replace cumbersome and restrictive DHP
139 equipment with miniaturized UAS technology capable of imaging the full 180° vertical
140 field of view and therefore retrieving vertical information related to canopy structural
141 traits, driving light and functional gradients within a plant canopy environment. To
142 validate our methodology, UAS-mounted spherical imagery was compared with
143 traditional DHP across species and stand types. To improve on DHP, vertical profiles of
144 PAD were derived, which were compared to airborne laser scanning data. Fig. 1 provides
145 an overview of the new method.

146 *Fig. 1: here*

147 **Materials and methods**

148 **Overview of measurements**

149 There were two main objectives to the data collection:

- 150 1. comparison of UAS-estimated PAI and gap fraction with DHP;
- 151 2. retrieval of vertical trait profiles using UAS.

152 To achieve these objectives, measurements were conducted at two sites in Finland during
153 spring and early summer 2021. The UAS was flown through mature Norway spruce
154 (*Picea abies* (L.) H. Karst), Scots pine (*Pinus sylvestris* L.) and silver/downy birch-
155 dominated (*Betula pendula* Roth/ *Betula pubescens* Ehrh) stands, taking spherical images
156 at different heights. Vertical profiles of PAI were used to derive PAD and compared to
157 airborne laser scanning (ALS) data, and DHP used to validate near ground imagery. Data
158 was collected at the Viikki Arboretum (Helsinki - 60.2° N 25.0 E) of the University of
159 Helsinki between February and April 2021, and in the surroundings of the Station for
160 Measuring Ecosystem-Atmosphere Relations II (SMEAR II), Hyytiälä (61.8 N, 24.3 E)
161 in May and June 2021. Spherical panoramic imagery was reprojected using a Python
162 script and analysed using Hemisfer software licensed version 3.1 (Patrick Schleppe, WLS
163 Swiss Federal Institute for Forest, Snow and Landscape research, Switzerland) to
164 optically derive the gap fraction and estimate PAI. The same software was used for the
165 DHP data.

166 **UAS description and camera calibration**

167 The mass-produced Parrot ANAFI was used to capture spherical panoramas (Parrot
168 Drones SAS, Paris, France). The ANAFI is compact (240 mm maximum dimension) and
169 lightweight (320 g), with a high-resolution camera (21 MP) capable of looking directly
170 upwards thanks to its 180° tilt gimbal (Fig.1). The main characteristics of the UAS are
171 found in Table 1.

172

173

UAS characteristics	
	Physical properties
Size unfolded	175x240x65 mm
Weight (take-off weight)	320 g
Max flight time (one battery)	25 min
Operating temperature range	-10° C to 40°C
Satellite Positioning Systems	GPS and GLONASS
	Imaging system
Sensor	1/2.4" CMOS: 5.9 x 4.43 mm
Lens	ASPH (Sharper images)
Aperture	f/2.4
Focal length (specifications)	Photo: 3.92 – 11.76 mm
Shutter speed	electronic shutter 1 to 1/10000 s
ISO range	100 - 3200
Image resolution	Wide
	21 MP (5344x4016) / 4:3 / 84° HFOV
	Rectilinear
	16MP (4608x3456) / 4:3 / 75.5° HFOV.
	IHFOV: 0.016° - IVFOV: 0.022°
Image formats	JPEG, DNG (raw)
	Stabilization
Image stabilization	3-axis hybrid: Mechanical - 2-axis Roll/Tilt angles; Electronic (EIS) - 3-axis Roll/Pan/Tilt angles
Gimbal tilt	Controllable - 90° to +90° (180° total)
	Additional information
Cost in 2021 (Finland)	650 – 800 Euro
Pending EULA class	C1

175

176 To calibrate the ANAFI camera, we followed the protocol found in the Hemisfer
 177 documentation (Schleppi *et al.*, 2007; Thimonier *et al.*, 2010). The output of the
 178 calibration is a lens function which characterizes radial distortion in the reprojected
 179 hemispherical image (see Notes S2 and Fig S1 in the Supplementary Information). This
 180 was performed outside under a small bridge, as the ANAFI stitching method failed
 181 indoors due to movement of the UAS. Minimal radial distortion was found in the UAS
 182 sensor hence we proceeded with the built-in linear lens function to analyse UAS imagery.

183 **UAS imagery acquisition and processing**

184 Each UAS-based spherical image was formed from 42 images in JPEG format taken
 185 automatically using the 360° image mode. These were stitched together using either the
 186 inbuilt Panorama mode in the FreeFlight 6 Parrot flight application (Parrot Drones SAS,
 187 Paris, France) or Microsoft Image Composition Editor (Microsoft Corporation, Redmont,
 188 WA, USA). The latter was used when FreeFlight 6 failed due to software processing
 189 errors. The resulting spherical images were in the equirectangular projection, where X-
 190 axis represents the azimuth angle and Y-axis the zenith angle (Fangi & Nardinocchi,
 191 2013). The built-in UAS sensors (gyroscope, compass and barometer) allow the spherical
 192 image to be accurately levelled, and thus the upper and lower half correspond to the upper
 193 and lower hemisphere (Li & Ratti, 2019). A Python script
 194 (<https://github.com/HowcanoeWang/Spherical2TreeAttributes>, Wang, 2019) was
 195 adapted to reproject panoramas to DHP equivalent imagery (see Notes S1). These UAS-
 196 based hemispherical images had a size of 4000 x 4000 pixels and a radius of 2000 pixels.

197 To process UAS imagery, we used the Hemisfer built-in linear lens function with a 90°
 198 field of view. The Nobis and Hunziker (2005) method was used to binarize the image into

199 black (plant material) and white (sky) pixels. It was binarized either manually or
200 following the Ridler & Calvard (1978) method when the former failed in open and
201 heterogenous sky conditions. The gamma value was set by default at 2.2 and all bands
202 of the RGB image were used. The gap fraction was calculated by dividing the
203 hemispherical image into 5 annuli of 15° and the Miller (Miller, 1967) method was used
204 for PAI. Shoot-level clumping was corrected by dividing the LAI by four times the mean
205 Silhouette to Total Area Ratio (STAR) (Oker-Blom & Smolander, 1988). A STAR value
206 of 0.147 was used for pine stands and 0.161 for spruce. Clumping correction was not
207 applied to birch (Majasalmi *et al.*, 2013) and we did not correct for stand level clumping.
208 We also did not the correct woody-to-non-woody ratio, as the purpose was not to achieve
209 accuracy in LAI estimation, but rather assess the relative accuracy of the UAS method.

210 For the UAS-DHP inter-comparison, UAS-imagery was taken at the same height as DHP,
211 as close in time as possible. After taking off and stabilizing the drone, the spherical image
212 protocol was started. Exposure settings were set to optimize the final image: ISO 200 and
213 light-dependent shutter speed (set to optimize first image), manually set looking at the
214 UAS histogram. Post-capture, images were inspected manually and then run through
215 Hemisfer to produce estimates of gap fraction and PAI.

216 DHP data collection for comparison with UAS imagery

217 We collected DHP imagery coincident with UAS-based spherical images and taken under
218 differing plant canopy architectures at both sites (total n=60). DHP images were taken
219 with a single lens reflex camera, an extreme-wide field of view fisheye-lens, a self-
220 levelling mount with circular bubble level and a tripod. The camera was a Canon EOS
221 70D (Canon Inc., Ōta, Tokyo, Japan). The fisheye lens was a Sigma 4.5 mm F2.8 EX DC
222 Circular Fisheye HSM (Sigma Corporation, Kawasaki, Kanawanga, Japan), with a full
223 180° field of view, a focal length of 17 - 55 mm and minimum aperture of F22. The self-
224 levelling mount was a Delta-T SLM9 (Delta-T Devices Ltd, Cambridge, UK) which was
225 mounted on the top of Slik Pro 400DX tripod (Slik Corporation, Hidaka, Hokkaido,
226 Japan).

227 The camera was mounted at 100 cm height from the ground, aligned towards magnetic
228 north and levelled. Exposure was optimised using the image histograms (Beckschäfer *et*
229 *al.*, 2013), exposing the image to the brightest pixels. ISO was set to a constant value of
230 200 to avoid grain, the sensor openness was also set to a constant value of F20/22
231 (Hartikainen *et al.*, 2018) and the focus was set to optimize the clarity and quality of the
232 image. As above, Hemisfer was used to process imagery. DHP imagery had a size of 3648
233 x 3648 pixels and radius of 1530 pixels and a vertical and horizontal Instantaneous Field
234 of View (H/VIFOV) of 0.118°. As with the UAS, the Hemisfer calibration protocol was
235 followed, and in this case we used the estimated lens function in our subsequent analysis
236 (Supplementary Information Fig. S1).

237 PAD estimation

238 To obtain vertical profiles of PAI and PAD we first selected suitable locations for flying
239 vertical profiles requiring canopy gaps of at least c12 m². Three repetitions of two profiles
240 per main species were conducted by taking three images at each height, starting at the
241 minimum flight height (<50 cm) and then flying upwards and stopping at 2 m increments.
242 PAI profiles were calculated as above using images taken at each measurement height.

243 We derived PAD profiles from adjacent-in-height PAI values using the following formula
 244 (Neumann *et al.* 1989):

$$245 \quad PAD \approx \frac{PAI_i - PAI_j}{z_j - z_i} \quad \text{Eqn. 2}$$

246 where i is the first layer (lower height) and j the second layer (upper height) and z is
 247 height from the ground.

248 Comparison of vertical PAD profiles to ALS data

249 We used ALS data to assess the accuracy of our PAI and PAD profiles. ALS acquisition
 250 took place June 3, 2020 using an aeroplane mounted Riegl Q1560 sensor ($\lambda = 1064$ nm).
 251 The scanning range was 1.2 km and the area was covered by three overlapping strips.
 252 Scan zenith angles were 1-24° and the pulse density was 40-60 pulses per m². The sensor
 253 operates two laser scanners. These had been calibrated to provide a 3D relative point
 254 match (approximate 68% precision) of better than 20 cm. This was verified against man-
 255 made targets such as power line cables. Each pulse transmitted resulted in 1-9 echoes
 256 (discrete points) with a minimal spacing (along the pulse) of c1.5 m.

257 To calculate a PAD proxy from LiDAR point cloud data, we first excluded points greater
 258 than 10 m radius from UAS profile location. Points below 1.5 m height were assigned as
 259 ground returns (N_g). Next the cylindrical point cloud was divided into 50 vertical
 260 segments which corresponded to an approximately 0.5 m height interval at each location.
 261 We used the ratio of points above each level to total returns, which included ground
 262 returns, from Solberg *et al.* (2006) to estimate transmission (T) through the canopy:

$$263 \quad T = 1 - \frac{N_c}{N_t} = 1 - \frac{N_c}{N_g + N_c} \quad \text{Eqn. 3}$$

264 where N_c is the returns above a certain height and N_t is the total number of returns. The
 265 following equation was then used to estimate ALS PAI:

$$266 \quad PAI = \frac{-1}{k} \cdot \ln(T) \quad \text{Eqn. 4}$$

267 in which k is the extinction coefficient value. (Note that Eqn. 4 is a modified form of Eqn.
 268 1 assuming T is equal to P). We estimated k and PAI from Eqn. 4 using ordinary least
 269 squares and UAS PAI measurements. The differential values of PAI throughout the
 270 canopy height were used to estimate the PAD values using Eqn. 2, and summary statistics
 271 were calculated between ALS and UAS PAD profiles.

272 Statistical and error analyses

273 Linear regression was used to analyse the relationship between DHP and UAS estimated
 274 traits. The coefficient of determination (R^2) and the regression standard error were
 275 calculated. The relative regression standard error (RSE) was calculated as:

$$276 \quad RSE = \frac{SE}{\bar{y}} \cdot 100 = \frac{\sqrt{\frac{1}{N-2} \cdot \sum_{i=1}^N (y_i - \hat{y}_i)^2}}{\bar{y}} \cdot 100 \quad \text{Eqn. 5}$$

278 where \bar{y} is the mean value of the DHP trait observations, y_i is the observed DHP values,
279 \hat{y}_i is each of the predicted UAS values and N is the number of observations, with the traits
280 either gap fraction or PAI.

281 We also investigated three categories of error in DHP and UAS images: exposure
282 variability, image resolution and stitching error. To investigate exposure errors, the
283 histogram values of each picture were analysed. The difference in mean value of the
284 pixels (using the blue band) for each image was related to the difference in gap fraction
285 between the DHP and UAS images. A relationship between these two values suggests
286 part of the unexplained variance of the model is attributable to exposure. Linear
287 regression analysis was used to quantify the relationship. Additionally, and for UAS
288 imagery only, we conducted repeated sampling at eight locations. This was needed, as for
289 UAS imagery the exposure was set at the start of the data collection and a single set of
290 panoramic imagery takes 2-3 minutes to collect.

291 Error could also have resulted from differences in image resolution between the two
292 systems, hence the computer vision algorithm *Structural Similarity Index Measure*
293 (*SSIM*) from the Scikit-image Python package (Van der Walt *et al.*, 2014) was used to
294 highlight differences between DHP and UAS imagery. Finally, we analysed stitching
295 error due to discontinuities in the matching of individual photos and in the spherical image
296 building process. These errors were defined qualitatively as unnatural vegetation or image
297 discontinuities, and four examples are shown in Fig. S2. To quantify this, all 60 UAS-
298 based hemispherical images were visually inspected to assess the relative importance of
299 this error. The percentage of photos with no error and more than 1 error was obtained, as
300 well as the average number of errors per image. To test the significance of the error, we
301 performed a Welch's t-test (significance level of 0.05) on the residuals of the linear
302 regressions between DHP and UAS-based imagery of gap fraction and PAI linear models,
303 split by the error rate (no error, or more than 1 error).

304 Results

305 Comparison of reprojected spherical imagery with on-the-ground 306 hemispherical imagery

307 Fig. 2 is a comparison of imagery taken using both systems under a mixed birch, pine,
308 and spruce canopy. Qualitatively, the UAS imagery is similar in composition to the DHP
309 system, yet there are also subtle differences such as the higher resolution of the UAS
310 image.

311 *Fig. 2: here.*

312 *Fig. 3: here.*

313 The main results of the comparison between the UAS-based method and the DHP datasets
314 are shown in Fig. 3. The coefficient of determination between the two methods was 0.89
315 for PAI and 0.92 for gap fraction across all annuli. The SE of the UAS-based PAI was

316 0.520 m²/m², which in percentage terms works out to an RSE of 24.2%; in terms of gap
 317 fraction estimation, the RSE was 16.1%.

318 Error analysis of gap fraction

319 We conducted an error analysis to pinpoint the cause of differences in DHP and UAS gap
 320 fraction and PAI estimates. Starting with exposure, we found a coefficient of
 321 determination of $R^2 = 0.64$ (Fig. 4) between mean pixel values and gap fraction
 322 differences between DHP and UAS, which signals a probable influence of exposure on
 323 the results. In Fig. 4, negative values indicate that DHP was underexposed relative to
 324 UAS and positive values indicate that DHP was overexposed relative to UAS.

325 *Fig. 4: here.*

326 Next, we analysed the replicability of gap fraction estimates in UAS imagery. Results
 327 showed that the variability between repetitions remained approximately constant at each
 328 location, with a median deviation of 3.4% for all locations (median of maximum deviation
 329 between the three measurements divided by its average, per each location). Most
 330 repetitions (87.5%) demonstrated a deviation in gap fraction of less than 10%.

331 The next source of error studied was the image resolution and resulting quality difference.
 332 The increased resolution of the UAS was evident when comparing images side-by-side
 333 (Fig. 2) and has been previously noted in reprojected panoramic imagery by Andis-Arietta
 334 (2021). Fig. 5 is a closer view of a small section of the example comparison imagery that
 335 highlights this issue and shows structural image differences, which are summarised by
 336 the SSIM value. Although UAS-based hemispherical image had an IFOV of 0.09°,
 337 whereas DHP had a value of 0.118°, in the analysis in Fig. 5 the UAS image was
 338 downsampled to the same number of pixels (IFOV) as the DHP. The quality difference
 339 persisted even when the number of pixels were set equal.

340 *Fig. 5: here.*

341 The final source of error studied was stitching error. We found that 50% of images were
 342 visually clear of errors, and the average number of errors per image was 1.07. The results
 343 of the Welch's T-test performed on the PAI and gap fraction residuals, grouped into a.
 344 errors present and b. no errors are shown in table 2. There were no statistically significant
 345 differences between the groups for PAI nor gap fraction.

346 *Table 2: Results of the statistical tests relating to panoramic stitching errors in plant area index (PAI) and gap fraction*
 347 *estimates.*

Statistics	Residuals PAI		Residuals gap fraction	
	No error	Error	No error	Error
Mean	0.0038	-0.0023	0.0025	-0.0025
Variance	0.2842	0.2597	0.0042	0.0040
p value (Welch's test, two tails)	0.964		0.765	

348

349 Vertical profiles of PAI and PAD

350 Next, we used the UAS method to retrieve vertical profiles of PAI and PAD in different
 351 canopies. Results are presented in Fig. 6, which shows six vertical profiles, two per

352 species, obtained in a Norway spruce stand, a Scots pine stand and a birch-dominated
353 stand. The figure also shows the ALS proxies of PAI and PAD.

354 *Fig. 6: here.*

355 UAS PAD profiles in the top row of Fig. 6 demonstrate the characteristic conical shape
356 of a dense Norway spruce stand. On the contrary, in *Pinus sylvestris* 1 and 2, the typical
357 lollipop-like elliptical profile of Scots pine is evident in the PAD estimate. The stand was
358 thinned in 2020, resulting in an opened stand, with a low PAI value and trees with few
359 branches below the height of the crown. Finally, the *Betula pendula* shown on the bottom
360 row of Fig. 6, differs in crown shape in comparison to the other two species. The birch
361 trees had longer and wider crowns compared to the pines.

362 ALS PAI and PAD proxy profiles are shown as grey lines in Fig. 6 and estimated ALS
363 extinction coefficients (k) and statistical summary results between the two methodologies
364 are presented in table 3. Estimated extinction coefficients were lowest in spruce (0.30,
365 0.35) and highest in birch (0.45, 0.61). Comparisons between ALS and UAS showed
366 similar PAD profile shapes across species, however there was some divergence at the
367 lower levels of the two spruce sites, which had the largest residual sum of squares between
368 ALS and UAS profiles.

369 *Table 3 Statistical analysis results of the ALS - UAS comparison. Note that in the statistical comparison, ALS plant*
370 *area density (PAD) values were calculated using the same height step size as the UAS PAD values.*

Profile	PAD residual sum of squares (m^2/m^3)	Height of maximum PAD residual (m)	k estimated
<i>Picea abies</i> 1	0.055	5	0.30
<i>Picea abies</i> 2	0.116	13	0.35
<i>Pinus sylvestris</i> 1	0.025	13	0.37
<i>Pinus sylvestris</i> 2	0.022	21	0.48
<i>Betula pendula</i> 1	0.008	7	0.45
<i>Betula pendula</i> 2	0.003	9	0.61

371

372 Discussion

373 Evaluation of UAS spherical photography

374 A major limitation of hemispherical photography is that it is usually restricted to ground-
375 based imagery, precluding the estimation of vertical traits. This limitation has stimulated
376 recent research into UAS-based hemispherical image collection (Brown *et al.*, 2020,
377 Brüllhardt *et al.*, 2020). Such systems use self-mounted cameras, that are potentially
378 problematic to fly under the forest canopy. On the contrary, the low-cost UAS used here
379 is small, lightweight and has an integrated imaging system that can produce upwards
380 looking imagery. Using our method, hemispherical fish-eye type images are reproduced
381 by utilizing a computational imaging technique, rather than the bulky DHP hardware
382 found in other studies. This raises the question: does the use of panoramic imagery result
383 in lower quality hemispherical imagery?

384 The correlations shown in Fig. 3 demonstrate that the spherical panorama-based
385 estimation of the gap fraction and PAI is very similar to that obtained by ground-based

386 hemispherical photography across a range of species and canopy structures. Nonetheless,
387 the differences in gap fraction and PAI between UAS and DHP imagery that we did find
388 were related to a number of factors common to both systems.

389 As expected, we found that exposure differences between systems had a non-negligible
390 effect on the gap fraction estimation (Fig. 4). Overexposure of imagery results in an
391 overestimation of gap fraction, as small branches or foliage elements are incorrectly
392 segmented as sky. An example of an overexposed DHP histogram is shown in the top left
393 corner inset of Fig. 4. There were also a few overexposed UAS images in the dataset, with
394 an example histogram shown inset into the lower right corner of Fig. 4. This inset graph
395 also shows an underexposed DHP histogram. Note that exposure can be difficult to set
396 correctly in panoramic imagery, as the parameters are set at the start of image collection
397 and then keep constant across all camera viewing angles. From our analysis, exposure
398 variability appeared to influence DHP and UAS imagery, however as we arrived at our
399 conclusions by comparing two uncalibrated cameras a note of caution is required.

400 A further issue related to exposure and UAS measurements, was our strong preference
401 for overcast days rather than clear dusks and dawns. This was because complete profiles
402 could take upwards of 40 minutes to collect, during which time dusk or dawn light
403 conditions substantially change. Raw format imagery could help with exposure and light
404 condition related errors (Macfarlane *et al.*, 2014; Hartikainen *et al.*, 2018) bypassing
405 automatic gamma correction performed by the camera, however custom software would
406 need to be developed for the UAS to collect raw format panoramas.

407 The lower quality of DHP imagery relative to the UAS resulted in a reduced number of
408 small gaps. Even when downsampling reprojected panoramic imagery to the same
409 number of pixels as DHP imagery, the angular resolution of the UAS was lower than the
410 DHP, resulting in a higher image quality. In the thresholded binary images, lower quality
411 leads to a greater proportion of misclassified pixels, and hence to an underestimation of
412 small gaps (Macfarlane, 2011; Andis-Arietta, 2021). This is known as *blooming*,
413 occurring when light saturation on the sensor spills over onto neighbouring pixels, and is
414 enhanced by overexposure which occurred in a few of our DHP images (Leblanc *et al.*,
415 2005). To summarise, the lower resolution of DHP results in a lower gap fraction and
416 accordingly, a higher PAI. This pattern was found to exist independently of canopy
417 species and structures.

418 Stitching errors were found to be of less importance than exposure or resolution. Though
419 generally high, stitching quality depended on the UAS stability when taking the
420 individual images. This was probably related to turbulence in the crown layer (Brüllhardt
421 *et al.* 2020). We therefore encourage careful inspection of imagery prior to gap fraction
422 estimation for stitching errors, such as those presented in Fig. S2. A final source of error
423 that we did not consider was reprojection error. In theory the spherical-to-hemispherical
424 transformation could cause errors or loss of information, especially in the top of the image
425 where the highest expansion and compression occurs.

426 We used reprojected imagery in our study for two reasons. First, it meant we could
427 compare imagery directly to that captured by a conventional DHP system. The second,
428 and related, reason was that we could use standard software, Hemisfer, to compute gap
429 fractions and PAI. Andis-Arietta (2021) stated the hemispherical reprojected is not a

430 requirement for PAI or gap fraction estimation from panoramas, but did not calculate gap
431 fractions directly from panoramic imagery. Wang (2019) did calculate gap fractions
432 directly from panoramic imagery, using an area-based weighting function to correct for
433 the cylindrical panoramic projection. Interestingly, and almost three decades ago,
434 Andrieu *et al.* (1994) calculated bidirectional gap fractions from panoramic-like imagery
435 reprojected from fisheye imagery, effectively inverting the projection applied here. Taken
436 together, these studies suggest a fruitful path forward is the development of software, and
437 appropriate theory, to operate directly on the common panoramic projections, and their
438 relation, the fisheye image.

439 Vertical profiles of canopy structural traits and ALS comparison

440 We retrieved vertical profiles of PAI and PAD by flying the UAS in canopy gaps.
441 Although more stable in heavy winds, it is unlikely that larger UASs carrying heavier
442 payloads (Brüllhardt *et al.*, 2020; Hyyppä *et al.*, 2021) can fly with a similar degree of
443 safety in such areas. However, before we can reach a potential gap size lower limit with
444 our UAS in the upper canopy, the issue of UAS drift requires attention.

445 UAS drift was a source of variability in vertical profiles of structural traits. When
446 ascending throughout the canopy, the UAS occasionally drifted from the starting location
447 in the horizontal plane. This was the main reason why big enough gaps were required
448 when choosing the sampling location. Between 6 and 10 m height, drifting was a critical
449 issue, as that height was where the largest crown diameter was situated. Drift is a potential
450 cause of stitching errors which show up as image discontinuities (Andis-Arietta, 2021)
451 related to alignment errors (Fangi & Nardinocchi, 2013). A further effect of drifting was
452 to change the sampling location at different heights, potentially altering the PAI value
453 and in extreme cases halting image collection. Further research should be done to better
454 understand the causes of UAS drifting behaviour and to program the UAS so that
455 spherical image collection would not stop even when the pilot manually changed the UAS
456 position.

457 To explore the effectiveness of our new method, we compared UAS-based spherical
458 photography derived PAD profiles to simple ALS estimated PAI and PAD proxies. In
459 general, pine, birch and spruce profiles were well matched between the UAS and ALS
460 approaches. Though dependant on the specific ALS instrumentation and proxy method
461 applied (Korhonen *et al.* 2011), estimated extinction coefficients were similar to literature
462 values, with the birch plots closest to the theoretical spherical leaf angle distribution
463 derived k of 0.5 (Lintunen *et al.* 2013). This is not surprising, as we used UAS imagery
464 to estimate extinction coefficients, but the parameter estimation does demonstrate a novel
465 use of the UAS profiles.

466 The largest errors between ALS and UAS PAD profiles occurred in the denser spruce
467 plots. Differences between ALS and UAS profiles could relate to a saturation effect at
468 higher LAI values (Tian *et al.* 2021b) or differences in the measurement geometries of
469 the two systems, including the effect of laser scan angles. The UAS samples a cone-like
470 area around the imaging system, whereas the ALS data were restricted to points collected
471 within a 10 m radius cylinder, centred at the UAS location (Fig. S3). Hence the laser
472 scanned surface was considerably smaller than the surface imaged from the UAS
473 (Korhonen *et al.*, 2011). This could have contributed to errors in the method comparison.

474 Using only the inner annuli of the UAS imagery could have potentially lessened the error
475 in the comparison (Solberg *et al.* 2006), however we deemed this step unnecessary based
476 on the strength of our results. Likewise, a more sophisticated PAD method could have
477 been applied (Hosoi & Omasa, 2006; Tian *et al.*, 2021b).

478 Expanding the horizons of UAS spherical imagery

479 The main advance of our method is the ability to capture under canopy imagery some
480 distance away from the researcher. Aside from the vertical profiles, there are several
481 interesting applications for this. Most obviously, the method can be used to produce
482 hemispherical photographs in previously inaccessible locations. A specific example from
483 our own research is the requirement for hemispherical photography adjacent to light
484 exposed upper crowns, where we were previously limited to locations with tower
485 infrastructure. Other examples of difficult to access locations include wetland canopies
486 that are partially flooded with water such as marshes, swamps, or mangroves, with the
487 UAS potentially piloted from a boat. Forests with thick understoreys are another example,
488 as are dangerous or pristine environments where human impact should be minimised,
489 keeping in mind that the range of any UAS is potentially restricted by battery capacity,
490 controller signal strength and local legislation.

491 There are several additional parameters that can be calculated from hemispherical or
492 panoramic photography that we did not investigate here. These include basal area
493 estimation (Wang *et al.*, 2021), leaf angle distribution (Qi *et al.*, 2019), the fraction of
494 vegetation cover or intercepted photosynthetically active radiation (Li *et al.* 2015).
495 Understorey (Law & Waring, 1994) or crop plant area index (Brown *et al.*, 2020) could
496 both be estimated with the lower portion of the spherical panorama. Above canopy
497 structure from motion photogrammetry, from which it is now possible to estimate LAI
498 profiles (Lin *et al.* 2021), could be complemented with within canopy spherical
499 photogrammetry (Fangi & Nardinocchi, 2013). Finally, a recent study showed the
500 potential of upward-looking thermal imaging to obtain canopy temperatures, which relate
501 to transpiration (Su *et al.*, 2020). A UAS thermal approach could be developed, with the
502 caveat that complementary visible imagery should be used for binarization.

503 Conclusions

504 We demonstrated a new method that used UAS-based spherical panoramic imagery to
505 estimate vertical profiles of PAI and PAD from canopies of different tree species and
506 structures. The method is inexpensive and safe relative to laser scanning and larger UAS
507 operation. The technique is complementary to laser scanning, which has a higher barrier
508 to entry (Calders *et al.* 2020), and is readily deployable by the working plant scientist.

509 Acknowledgements

510 JA was funded by Academy of Finland BiBiFe project (grant no: 324259). MD was
511 funded by Academy of Finland (grant no: 324555). We thank the three anonymous
512 reviewers whose comments helped to improve our study.

513 **Contributions**

514 VARC wrote the manuscript, performed the analyses, and carried out the field work. MD
515 and TMR contributed to the manuscript revision and guided the analyses. APC planned
516 the field sampling with VARC and contributed to conceptualization and manuscript
517 revisions. IK provided ALS data, helped with statistical analyses and contributed to the
518 manuscript. JA conceptualized the study, supervised VARC and helped VARC to write
519 the manuscript.

520 **Data availability**

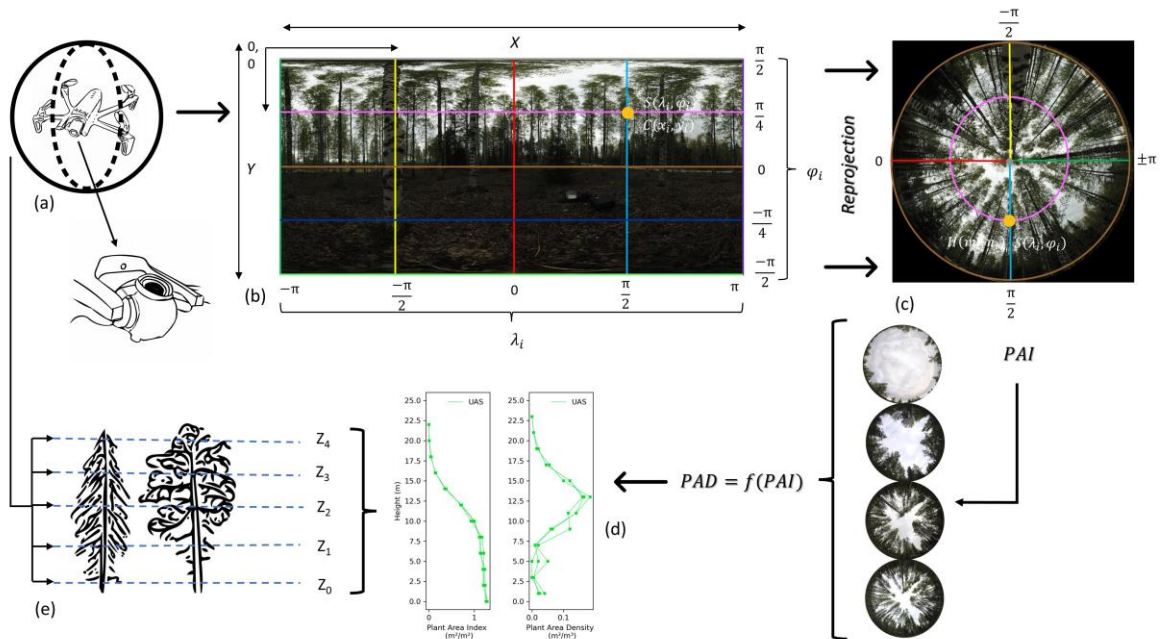
521 Data and processing scripts associated with the study were deposited on Zenodo under
522 DOI [10.5281/zenodo.5877899](https://doi.org/10.5281/zenodo.5877899)

523

524

525

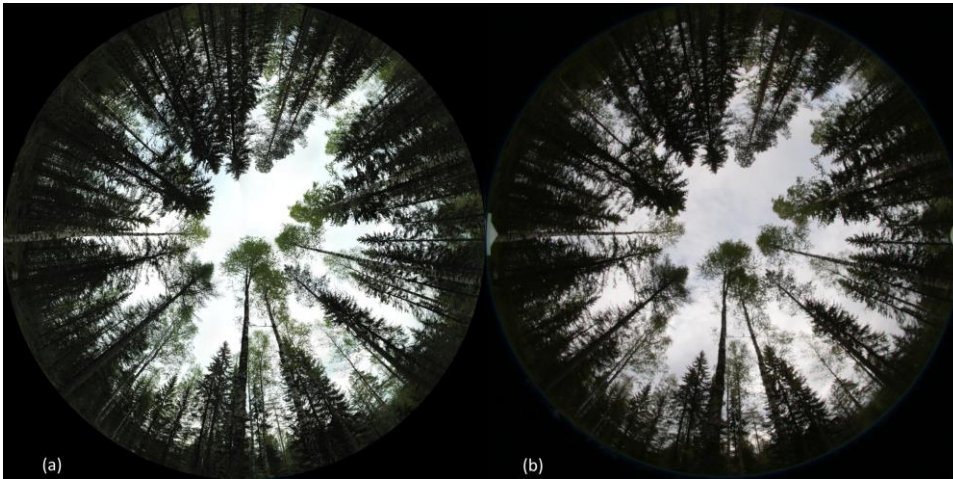
526



529

530 *Fig. 1: Schematic of the uncrewed aircraft system (UAS) spherical photographic method. The UAS (a) takes spherical*
 531 *panoramas (b) using its gimbal, that are reprojected to hemispherical upward-looking images (c) using the upper*
 532 *hemisphere ($\varphi > 0$). The UAS is flown at different heights of the canopy (e) and therefore a vertical distribution of the*
 533 *trait, e.g. plant area index and density (PAI, PAD), is obtained (d). For details on the reprojection see Notes S1 in the*
 534 *Supporting Information.*

535



537

538

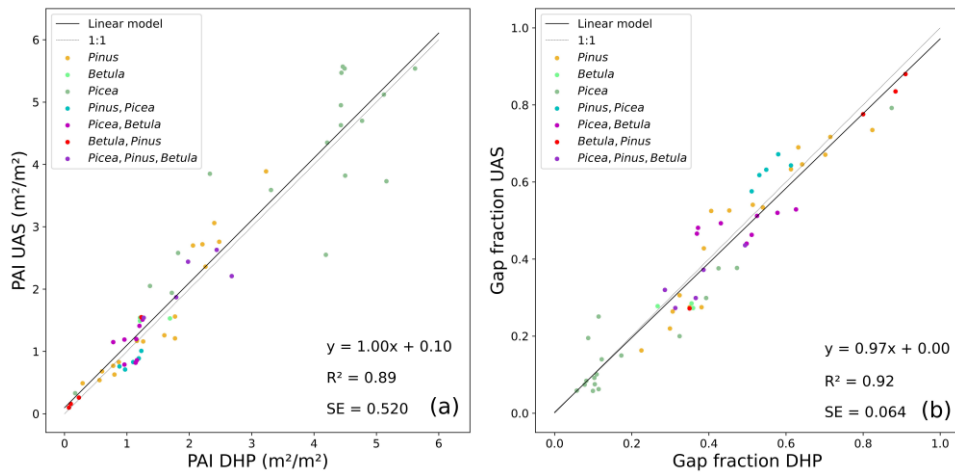
539

540

Fig. 2: Example comparison of hemispherical imagery using the two differing approaches: (a) is an image from the uncrewed aircraft system (UAS) and (b) is the digital hemispherical photography (DHP) image. Images were taken in May 2021 close to Hyttiälä SMEAR II station, in a thinned stand of Scots pine, birch and Norway spruce.

541

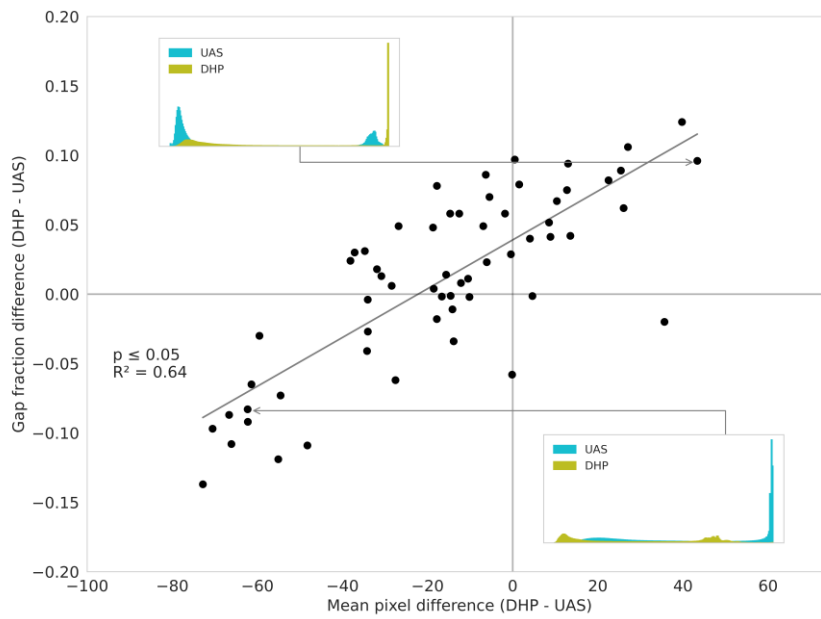
542



543

544 *Fig. 3: Comparison between the uncrewed aircraft system (UAS) and Digital Hemispherical Photography (DHP)*
545 *derived plant area index (PAI) (a) and gap fraction (b). A total of 60 locations (n=60) were selected, of which 22 pairs*
546 *of images were in Viikki Arboretum. The following canopy structures were represented: open field, unthinned dense*
547 *Norway spruce, mixed Scots pine and birch, pure birch, mature Scots pine, Norway spruce and birch and thinned pure*
548 *Scots pine.*

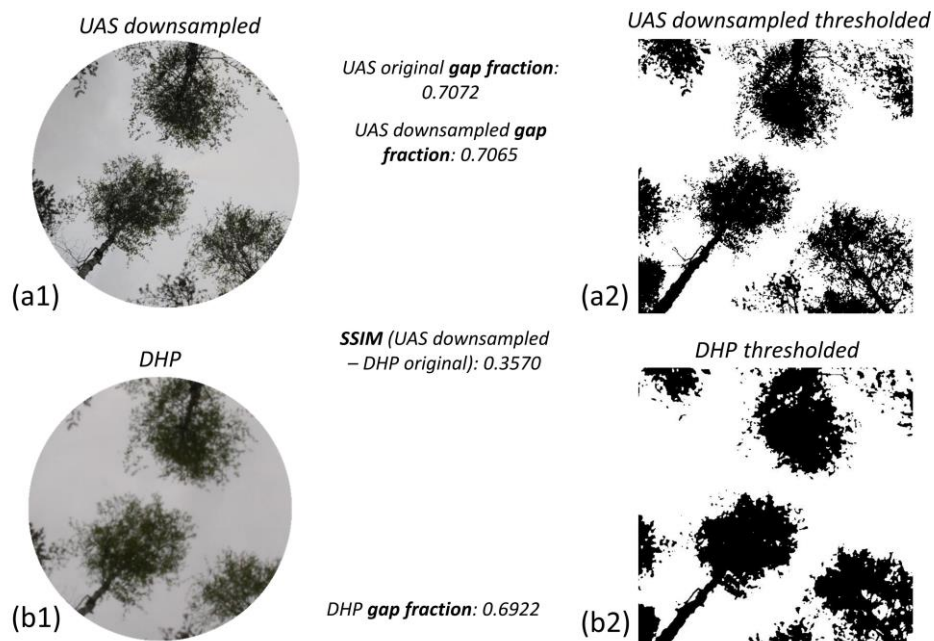
549



551

552 *Fig. 4: Relationship between gap fraction difference and the histogram mean pixel value difference between the digital*
 553 *hemispherical photographic (DHP) imagery and the uncrewed aircraft system (UAS) imagery for the blue channel.*
 554 *The inset plots are examples of blue channel image histograms, with values from 0 to 255, demonstrating overexposure*
 555 *in each of the two systems.*

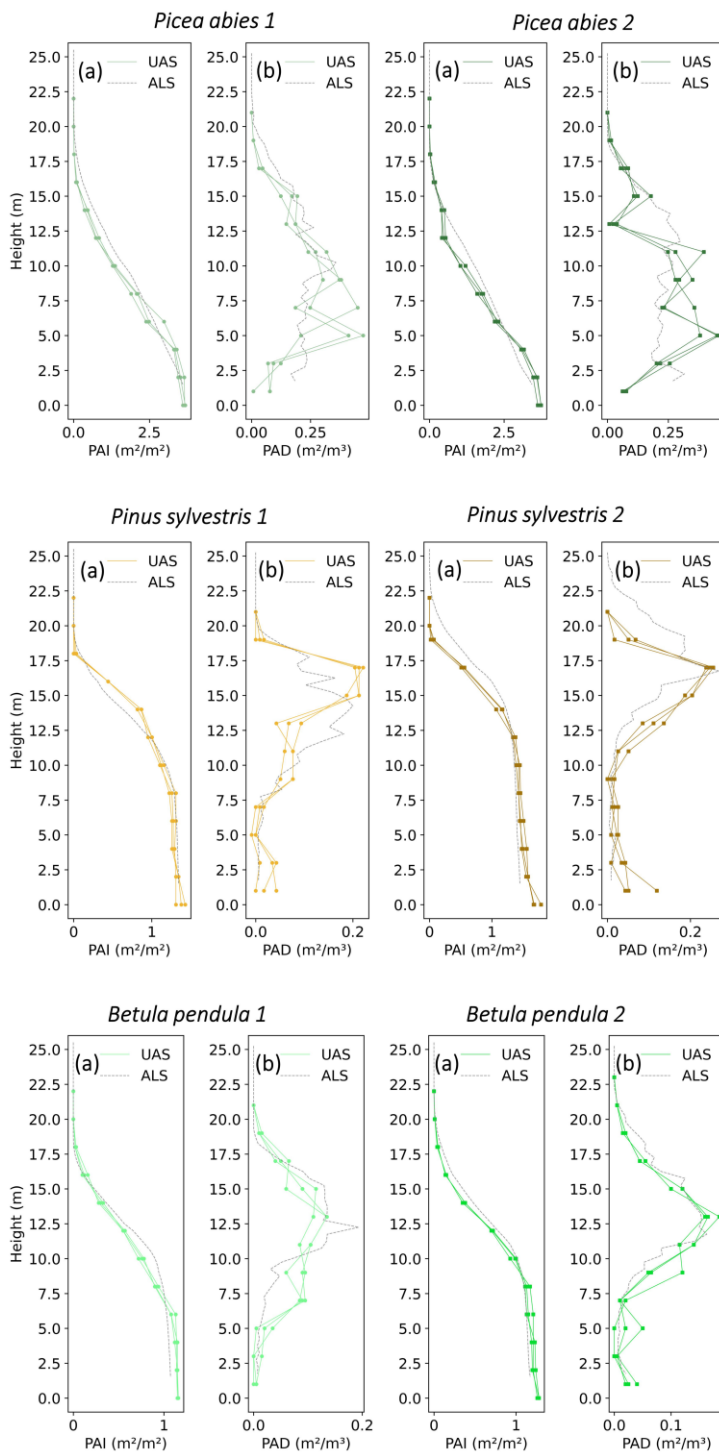
556



558

559 *Fig. 5: Detail of the comparison of the first annulus of two images (zenith angle between 0 and 15°). Top row, uncrewed*
 560 *aircraft system (UAS) downsampled image (a) and bottom row, digital hemispherical photography (DHP) image (b).*
 561 *From left to right: direct sub-image comparison (a1, b1) and comparison of the binarized image (a2, b2). The gap*
 562 *fraction for each sub-image was obtained, as well as the Structural Similarity Index Measure (SSIM), in order to*
 563 *quantitatively compare both images. The UAS image was downsampled to the same number of pixels as the DHP*
 564 *image.*

565



567

568 *Fig. 6: Vertical profiles obtained from uncrowded aircraft system (UAS) spherical imagery (continuous lines) and*
 569 *airborne laser scanning (ALS) data (grey dashed lines). Each subfigure shows two different profiles in a Picea abies*
 570 *stand, Pinus sylvestris stand and Betula pendula dominated stand. Letters represent the cumulative plant area index*
 571 *(PAI) (a) and plant area density (PAD) (b) vertical distribution. In each profile location, three repetitions (spherical*
 572 *photos) were taken per layer (height).*

573

574 **References**

- 575 **Andis-Arietta AZ. 2021.** Estimation of forest canopy structure and understory light using
576 spherical panorama images from smartphone photography. *Forestry*. **Cpab034**: 1-11.
- 577 **Andrieu, B, Sohbi Y, Ivanov, N. 1994.** A direct method to measure bidirectional gap
578 fraction in vegetation canopies. *Remote Sensing of Environment* **50**: 61-66.
- 579 **Barbero-García I, Cabrelles M, Lerma JL, Marqués-Mateu A. 2018.** Smartphone-
580 based close-range photogrammetric assessment of spherical objects. *The*
581 *Photogrammetric Record* **33**: 283-299
- 582 **Beckschäfer P, Seidel D, Kleinn C, Xu J. 2013.** On the exposure of hemispherical
583 photographs in forests. *iForest – Biogeosciences* **6**: 228-237
- 584 **Brede B, Calders K, Lau A, Raunonen P, Bartholomeus HM, Herold M, Kooistra**
585 **L. 2019.** Non-destructive tree volume estimation through quantitative structure
586 modelling: Comparing UAV laser scanning with terrestrial LIDAR. *Remote Sensing of*
587 *Environment* **233**: 111335
- 588 **Brown LA, Sutherland DH, Dash J. 2020.** Low-cost unmanned aerial vehicle-based
589 digital hemispherical photography for estimating leaf area index: a feasibility assessment.
590 *International Journal of Remote Sensing* **41**: 9064-9074.
- 591 **Brüllhardt M, Rotach P, Schleppi P, Bugmann H. 2020.** Vertical light transmission
592 profiles in structured mixed deciduous forest canopies assessed by UAV-based
593 hemispherical photography and photogrammetric vegetation height models. *Agricultural*
594 *and Forest Meteorology* **281**: 107843.
- 595 **Calders K, Adams J, Armston J, Bartholomeus H, Bauwens S, Bentley LP, Chave J,**
596 **Danson FM, Demol M, Disney M, et al. 2020.** Terrestrial laser scanning in forest
597 ecology: Expanding the horizon. *Remote Sensing of Environment* **251**: 112102.
- 598 **Canham CD, Finzi AC, Pacala SW, Burbank DH. 1994.** Causes and consequences of
599 resource heterogeneity in forests: interspecific variation in light transmission by canopy
600 trees. *Canadian Journal of Forest Research* **24**: 337-359.
- 601 **Chen JM, Black TA, Adams RS. 1991.** Evaluation of hemispherical photography for
602 determining plant area index and geometry of a forest stand. *Agricultural and Forest*
603 *Meteorology* **56**: 129-143.
- 604 **Chianucci F, Cutini A. 2012.** Digital hemispherical photography for estimating forest
605 canopy properties: current controversies and opportunities. *iForest – Biogeosciences and*
606 *Forestry* **5**: 290-295.
- 607 **Chianucci F. 2020.** An overview of in situ digital canopy photography in forestry.
608 *Canadian Journal of Forest Research* **50**: 227-242.
- 609 **Cleugh HA, Leuning R, Mu Q, Running SW. 2007.** Regional evaporation estimates
610 from flux tower and MODIS satellite data. *Remote Sensing Environment* **106**: 285-304.

- 611 **Danson FM, Hetherington D, Morsdorf F, Koetz G, Allgöwer B. 2007.** Forest canopy
612 gap fraction from terrestrial laser scanning. *IEEE Geoscience and remote sensing letters*
613 **4**: 157-160.
- 614 **Dengel S, Grace J, MacArthur A. 2015.** Transmissivity of solar radiation within a *Picea*
615 *sitchensis* stand under various sky conditions. *Biogeosciences* **12**: 4195-4207.
- 616 **Dietz J, Hölscher D, Leuschnerb C, Hendrayanto. 2006.** Rainfall partitioning in
617 relation to forest structure in differently managed montane forest stands in Central
618 Sulawesi, Indonesia. *Forest Ecology and Management* **237**: 170-178.
- 619 **Disney, M. 2019.** Terrestrial LiDAR: a three-dimensional revolution in how we look at
620 trees. *New Phytologist* **222**: 1736-1741.
- 621 **Duchemin B, Hadriab R, Errakib S, Bouleta G, Maisongrandea P, Chehbounia A,**
622 **Escadafala R, Ezzaharb, Hoedjesa JCB, Kharroud MH et al. 2006.** Monitoring wheat
623 phenology and irrigation in Central Morocco: On the use of relationships between
624 evapotranspiration, crops coefficients, leaf area index and remotely-sensed vegetation
625 indices. *Agricultural Water Management* **79**: 1-27.
- 626 **Fangi G, Nardinocchi C. 2013.** Photogrammetric Processing of Spherical Panoramas.
627 *The Photogrammetric Record* **28**: 293-311.
- 628 **Fauset S, Gloor MU, Aidar MPM, Freitas HC, Fyllas NM, Marabesi MA, Rochelle**
629 **ALC, Shenkin A, Vieira SA, Joly CA. 2017.** Tropical forest light regimes in a human-
630 modified landscape. *Ecosphere* **8**: e02002.
- 631 **Frazer GW, Fournier RA, Trofymow JA, Hall RJ. 2001.** A comparison of digital and
632 film fisheye photography for analysis of forest canopy structure and gap light
633 transmission. *Agricultural and Forest Meteorology* **109**: 249-263.
- 634 **Glatthorn J, Beckschäfer P. 2014.** Standardizing the protocol for hemispherical
635 photographs. Accuracy assessment of binarization algorithms. *PLOS ONE* **9**: e111924.
- 636 **Guangjian Y, Ronghai H, Jinghui L, Marie W, Halian J, Xihan M, Donghui X,**
637 **Wuming Z. 2019.** Review of indirect optical measurements of leaf area index: Recent
638 advances, challenges, and perspectives. *Agricultural and Forest Meteorology* **265**: 390-
639 411.
- 640 **Hartikainen SM, Jach A, Grané A, Robson TM. 2018.** Assessing scale-wise similarity
641 of curves with a think pen: As illustrated through comparisons of spectral irradiance.
642 *Ecology and Evolution* **8**: 10206-10218.
- 643 **Hosoi F, Omasa K. 2006.** Voxel-Based 3-D Modeling of Individual Trees for Estimating
644 Leaf Area Density Using High-Resolution Portable Scanning Lidar. *IEEE Transactions*
645 *on Geoscience and Remote Sensing* **44**: 3610-3618.
- 646 **Hyypä J, Yu X, Hakala T, Kaartinen H, Kukko A, Hyyti H, Muhojoki J, Hyypä**
647 **E. 2021.** Under-Canopy UAV Laser Scanning Providing Canopy Height and Stem Volume
648 Accurately. *Forests* **12**: 856.

- 649 **Jonckheere I, Fleck S, Nackaerts K, Muys B. 2004.** Review of methods for in situ leaf
650 area index determination: Part I. Theories, sensors and hemispherical photography.
651 *Agricultural and Forest Meteorology* **121**: 19-35.
- 652 **Jongschaap REE. 2006.** Run-time calibration of simulation models by integrating
653 remote sensing estimates of leaf area index and canopy nitrogen. *European Journal of*
654 *Agronomy* **24**: 316-324.
- 655 **Korhonen L, Korpela I, Heiskanen J, Maltamo M. 2011.** Airborne discrete-return
656 LIDAR data in the estimation of vertical canopy cover, angular canopy closure and leaf
657 area index. *Remote Sensing of Environment* **115**: 1065-1080.
- 658 **Korpela I, Mehtätalo L, Markelin L, Seppänen A, Kangas A. 2014.** Tree species
659 identification in aerial image data using directional reflectance signatures. *Silva Fennica*
660 **48**: 1087.
- 661 **Krisanski S, Taskhiri MS, Turner P. 2020.** Enhancing Methods for Under-Canopy
662 Unmanned Aircraft System Based Photogrammetry in Complex Forests for Tree
663 Diameter Measurement. *Remote Sensing* **12**: 1652.
- 664 **Lalic B, Mihailovic DT. 2004.** An Empirical Relation Describing Leaf-Area Density
665 inside the Forest for Environmental modelling. *Journal of Applied Meteorology and*
666 *Climatology* **43**: 641-645.
- 667 **Law BE, Waring RH. 1994.** Remote sensing of leaf area index and radiation intercepted
668 by understory vegetation. *Ecological Applications* **4**: 272-279.
- 669 **Leblanc SG, Chen JM, Fernandes R, Deering DW, Conley A. 2005.** Methodology
670 comparison for canopy structure parameters extraction from digital hemispherical
671 photography in boreal forests. *Agricultural and Forest Meteorology* **129**: 187-207.
- 672 **Leblanc SG, Chen JM. 2001.** A practical scheme for correcting multiple scattering
673 effects on optical LAI measurements. *Agricultural and Forest Meteorology* **110**: 125-
674 139.
- 675 **Leuchner M, Hertel C, Menzel A. 2011.** Spatial variability of photosynthetically active
676 radiation in European beech and Norway spruce. *Agricultural and Forest Meteorology*
677 **151**: 1226-1232.
- 678 **Li W, Weiss M, Waldner F, Defourny P, Demarez V, Morin D, Hagolle O, Baret F.**
679 **2015.** A Generic Algorithm to Estimate LAI, FAPAR and FCOVER Variables from
680 SPOT4_HRVIR and Landsat Sensors: Evaluation of the Consistency and Comparison
681 with Ground Measurements. *Remote Sensing* **7**: 15494-15516.
- 682 **Li X, Ratti C. 2019.** Mapping the spatio-temporal distribution of solar radiation within
683 street canyons of Boston using Google Street View panoramas and building height model.
684 *Landscape and Urban Planning* **191**: 103387.
- 685 **Lim K, Treitz P, Baldwin K, Morrison I, Green J. 2003.** Lidar remote sensing of
686 biophysical properties of tolerant northern hardwood forests. *Canadian Journal of*
687 *Remote Sensing* **29**: 658-678.

- 688 **Lin L, Yu K, Yao X, Deng Y, Hao Z, Chen Y, Wu N, Liu J. 2021.** UAV Based
689 Estimation of Forest Leaf Area Index (LAI) through Oblique Photogrammetry. *Remote*
690 *Sensing* **13**: 803.
- 691 **Lintunen A, Kaitaniemi P, Perttunen J, Sievänen R. 2013.** Analysing species-specific
692 light transmission and related crown characteristics of *Pinus sylvestris* and *Betula*
693 *pendula* using a shoot-level 3D model. *Canadian Journal of Forest Research* **43**: 929-
694 938.
- 695 **Lovell JJ, Jupp DLP, Culvenor DS, Coops NC. 2003.** Using airborne and ground-based
696 ranging lidar to measure canopy structure in Australian forests. *Canadian Journal of*
697 *Remote Sensing* **29**: 607-622.
- 698 **Macfarlane C, Coote M, White DA, Adams MA. 2000.** Photographic exposure affects
699 indirect estimation of leaf area in plantations of *Eucalyptus globulus* Labill. *Agricultural*
700 *and Forest Meteorology* **100**: 155-168.
- 701 **Macfarlane C, Hoffman M, Eamus D, Kerp N, Higginson S, Mcmurtrie R, Adams**
702 **M. 2007.** Estimation of leaf area index in eucalypt forest using digital photography.
703 *Agricultural and Forest Meteorology* **143**: 176-188.
- 704 **Macfarlane C, Ryu Y, Ogden GN, Sonnentag O. 2014.** Digital canopy photography:
705 exposed and in the raw. *Agriculture and Forest Meteorology* **197**: 244-253.
- 706 **Macfarlane C. 2011.** Classification method of mixed pixels does not affect canopy
707 metrics from digital images of forest overstorey. *Agricultural and Forest Meteorology*
708 **151**: 833-840.
- 709 **Majasalmi T, Rautiainen M, Stenberg P, Lukeš. 2013.** An assessment of ground
710 reference methods for estimating LAI of boreal forests. *Forest Ecology and Management*
711 **292**: 10-18.
- 712 **Majasalmi T. 2015.** *Estimation of leaf area index and the fraction of absorbed*
713 *photosynthetically active radiation in a boreal forest.* PhD Thesis, Department of Forest
714 Sciences, Faculty of Agriculture and Forestry, University of Helsinki, Helsinki, Finland.
- 715 **McNeil BE, Pisek J, Lepisk H, Flamenco EA. 2016.** Measuring leaf angle distribution
716 in broadleaf canopies using UAVs. *Agricultural and Forest Meteorology* **218-219**: 204-
717 208.
- 718 **Meir P, Grace J, Miranda AC. 2000.** Photographic method to measure the vertical
719 distribution of leaf area density in forests. *Agricultural and Forest Meteorology* **102**: 105-
720 111.
- 721 **Miller J. 1967.** A formula for average foliage density. *Australian Journal of Botany* **15**:
722 141-144.
- 723 **Neumann HH, Den Hartog G, Shaw, RH. 1989.** Leaf area measurements based on
724 hemispheric photographs and leaf-litter collection in a deciduous forest during autumn
725 leaf-fall. *Agricultural and Forest Meteorology* **45**: 325-345.
- 726 **Nilson T. 1971.** A theoretical analysis of the frequency of gaps in plant stands.
727 *Agricultural and Forest Meteorology* **8**: 25-38.

- 728 **Nobis M, Hunziker U. 2005.** Automatic thresholding for hemispherical canopy-
729 photographs based on edge detection. *Agricultural and Forest Meteorology* **128**: 243-
730 250.
- 731 **Oker-Blom P, Smolander H. 1988.** The ratio of shoot silhouette area to total needle area
732 in Scots Pine. *Forest Science* **4**: 894-906.
- 733 **Parker GG, Lefsky MA, Harding DJ. 2001.** Light transmittance in forest canopies
734 determined using airborne laser altimetry and in-canopy quantum measurements. *Remote*
735 *Sensing of Environment* **76**: 298-309.
- 736 **Qi J, Xie D, Li L, Zhang W, Mu W, Yan G. 2019.** Estimating Leaf Angle Distribution
737 From Smartphone Photographs. *IEEE Geoscience and Remote Sensing Letters* **16**: 1190-
738 1194.
- 739 **Ridler TW, Calvard S. 1978.** Picture Thresholding Using an Iterative Selection Method.
740 *IEEE Transactions on Systems, Man, and Cybernetics* **8**: 630-632.
- 741 **Schleppi P, Conedera M, Sedivy I, Thimonier A. 2007.** Correcting non-linearity and
742 slope effects in the estimation of the leaf area index of forests from hemispherical
743 photographs. *Agriculture and Forest Meteorology* **144**: 236-242.
- 744 **Smith MN, Stark SC, Taylor TC, Ferreira ML, Oliveira E, Restrepo-Coupe R, Chen**
745 **S, Woodcock T, Benetes dos Santos D, Alves LF et al. 2019.** Seasonal drought-related
746 changes in leaf area profiles on height and light environment in an Amazon forest. *New*
747 *Phytologist* **222**: 1284-1297.
- 748 **Solberg S, Næsset E, Hansen KH, Christiansen E. 2006.** Mapping defoliation during a
749 severe insect attack on Scot's pine using airborne laser scanning. *Remote sensing of*
750 *Environment* **102**: 364-376.
- 751 **Su A, Qi J, Huang H. 2020.** Indirect Measurement of Forest Canopy Temperature by
752 Handheld Thermal Infrared Imager through Upward Observation. *Remote Sensing* **12**:
753 3559.
- 754 **Thimonier A, Sedivy I, Schleppi P. 2010.** Estimating leaf area index in different types
755 of mature forest stands in Switzerland: A comparison of methods. *European Journal of*
756 *Forest Research* **129**: 543-562.
- 757 **Tian S, Zheng G, Eitel JU, Zhang Q. 2021a.** A Lidar-Based 3-D Photosynthetically
758 Active Radiation Model Reveals the Spatiotemporal Variations of Forest Sunlit and
759 Shaded Leaves. *Remote Sensing* **13**: 1002.
- 760 **Tian L, Qu Y, Qi, J. 2021b.** Estimation of Forest LAI Using Discrete Airborne LiDAR:
761 A Review. *Remote Sensing* **13**: 2408.
- 762 **Umarhadi DA, Danoedoro P. 2021.** Comparing canopy density measurement from
763 UAV and hemispherical photography: an evaluation for medium resolution of remote
764 sensing-based mapping. *International Journal of Electrical and Computer Engineering*
765 *(IJECE)* **11**: 356-364.
- 766 **Van der Walt S, Schönberger JL, Nunez-Iglesias J, Boulogne F, Warner JD, Yager**
767 **N, Gouillart E, Yu T. 2014.** Scikit-image: image processing in Python. *PeerJ* **2**: e453.

- 768 **Wagner S. 1998.** Calibration of grey values of hemispherical photographs for image
769 analysis. *Agricultural and Forest Meteorology* **90**: 103-117.
- 770 **Wallace L, Lucieer LA, Watson C, Turner D. 2012.** Development of a UAV-LiDAR
771 System with Application to Forest Inventory. *Remote Sensing* **4**: 1519-1543.
- 772 **Wang H, Yang TR, Waldy J, Kershaw JA Jr. 2021.** Estimating Individual Tree Heights
773 and DBHS from Vertically Displaced Spherical Image Pairs. *Mathematical and*
774 *Computational Forestry & Natural-Resource Sciences* **13**: 0-13.
- 775 **Wang H. 2019.** *Estimating forest attributes from spherical images.* Master's Thesis.
776 Faculty of Forestry and Environmental Management, University of New Brunswick, NB,
777 Canada.
- 778 **Yin D, Wang L. 2019.** Individual mangrove tree measurement using UAV-based LiDAR
779 data: Possibilities and challenges. *Remote Sensing of Environment* **223**: 34-49.
- 780 **Zhang Y, Huang F. 2021.** Panoramic Visual SLAM Technology for Spherical Images.
781 *Sensors* **21**: 705.
- 782 **Zheng G, Moskal LM. 2009.** Retrieving Leaf Area Index (LAI) Using Remote Sensing:
783 Theories, Methods and Sensors. *Sensors* **9**: 2719-2745.

784 **Supporting Information**

- 785 **Notes S1** Panoramic reprojection to fisheye imagery.
- 786 **Notes S2** Calibration of the imaging sensors.
- 787 **Fig. S1** Calibration functions for both sensors.
- 788 **Fig. S2** Four examples of UAS panoramic stitching error.
- 789 **Fig. S3** ALS plot point clouds and ground level UAS imagery.
- 790 **Notes S3** Supporting Information references.